Growth, Structure, Spectroscopy, and Laser Operation of a "Mixed" Yb:(Y,Lu)3Al5O12 Garnet Crystal

Sami Slimi, Pavel Loiko, Mingyan Pan, Pauline Lehoux, Venkatesan Jambunathan, Martin Smrz, Tomas Mocek, Yicheng Wang, Weidong Chen, Valentin Petrov, et al.

crystals

MDPI

Article

Growth, Structure, Spectroscopy, and Laser Operation of a "Mixed" Yb:$(Y,Lu)_3Al_5O_{12}$ Garnet Crystal

Sami Slimi [1], Pavel Loiko [2], Mingyan Pan [3], Pauline Lehoux [2,4], Venkatesan Jambunathan [5], Martin Smrz [5], Tomas Mocek [5], Yicheng Wang [6], Weidong Chen [7], Valentin Petrov [8], Rosa Maria Solé [1], Magdalena Aguiló [1], Francesc Díaz [1], Patrice Camy [2] and Xavier Mateos [1,*,†]

[1] Física i Cristal·lografia de Materials (FiCMA), Universitat Rovira i Virgili (URV), Marcel·li Domingo 1, 43007 Tarragona, Spain; sami.slimi@urv.cat (S.S.)
[2] Centre de Recherche sur les Ions, les Matériaux et la Photonique (CIMAP), UMR 6252 CEA-CNRS-ENSICAEN, Université de Caen Normandie, 6 Boulevard Maréchal Juin, 14050 Caen, France
[3] Key Laboratory of Materials for High Power Laser, Shanghai Institute of Optics and Fine Mechanics, Chinese Academy of Sciences, Shanghai 201800, China
[4] Institut FOTON-UMR 6082, CNRS, Université Rennes, 35000 Rennes, France
[5] HiLASE Centre, Institute of Physics, Czech Academy of Sciences, Za Radnicí 828, 252 41 Dolní Břežany, Czech Republic
[6] Photonics and Ultrafast Laser Science, Ruhr Universität Bochum, Universitätsstrasse 150, 44801 Bochum, Germany
[7] Fujian Institute of Research on the Structure of Matter, Chinese Academy of Sciences, Fuzhou 350002, China
[8] Max Born Institute for Nonlinear Optics and Short Pulse Spectroscopy, Max-Born-Str. 2a, 12489 Berlin, Germany
* Correspondence: xavier.mateos@urv.cat
† Serra Húnter Fellow, Spain.

Abstract: A single crystal of ytterbium-doped "mixed" yttrium–lutetium aluminum garnet with a stoichiometric composition of $(Y_{0.601}Lu_{0.233}Yb_{0.166})_3Al_5O_{12}$ was grown by the Czochralski method and its structure, vibronic, spectroscopic, and laser properties were studied. The stimulated-emission cross-section for Yb^{3+} ions was maximized to 2.53×10^{-20} cm^2 at 1031 nm. The emission bandwidth was ~8 nm, and the reabsorption-free luminescence lifetime of the $^2F_{5/2}$ state was 1.063 ms. Pumped at 941 nm, the Yb laser generated a maximum output power of 1.04 W at 1.03 and 1.05 μm with a high slope efficiency of 76.4% and a laser threshold of 76 mW. A continuous wavelength tuning over a range of 51.6 nm (1026.4–1078.0 nm) was also achieved. Power scaling was achieved using a 969 nm diode-pumped microchip cavity. A maximum output power of ~9 W was obtained at 1.05 μm with a slope efficiency of 76% and an almost circular laser beam profile.

Keywords: garnet crystals; ytterbium ion; crystal structure; optical spectroscopy; solid-state lasers

Citation: Slimi, S.; Loiko, P.; Pan, M.; Lehoux, P.; Jambunathan, V.; Smrz, M.; Mocek, T.; Wang, Y.; Chen, W.; Petrov, V.; et al. Growth, Structure, Spectroscopy, and Laser Operation of a "Mixed" Yb:$(Y,Lu)_3Al_5O_{12}$ Garnet Crystal. *Crystals* **2023**, *13*, 1588. https://doi.org/10.3390/cryst13111588

Academic Editors: Maria Milanova and Martin Tsvetkov

Received: 24 October 2023
Revised: 10 November 2023
Accepted: 12 November 2023
Published: 15 November 2023

1. Introduction

The Ytterbium ion (Yb^{3+}) is a highly desirable choice for creating lasers that emit light at 1 μm. With its electronic configuration $[Xe]4f^{13}$, it possesses a straightforward energy-level structure consisting of just two sets (the ground state $^2F_{7/2}$ and the excited state $^2F_{5/2}$). This characteristic results in inherently high laser efficiency and minimal heat generation during in-band pumping. The Yb^{3+} ion's absorption can be conveniently addressed using commercially available high-power fiber-coupled InGaAs laser diodes that emit light at 0.94–0.98 μm. Additionally, the significant separation in energy levels of the ground state ($^2F_{7/2}$) makes Yb^{3+}-doped crystals exceptionally well-suited for generating ultra-short (femtosecond) pulses in mode-locked lasers.

Yttrium aluminum garnet (Chemical formula $Y_3Al_5O_{12}$), commonly known as YAG, is a cutting-edge crystal that can be doped with Yb^{3+} ions to enable efficient laser emission around 1 μm [1,2]. YAG possesses favorable thermal, mechanical, and thermo-optical

characteristics [3], and it allows for straightforward Yb^{3+} doping at high concentrations (10 at.% and higher). Moreover, it has a well-established growth method using the Czochralski technique. YAG crystallizes in a cubic structure (space group Ia3d) with a single rare-earth site (D_2 symmetry and VIII-fold oxygen coordination). Yb: YAG crystals are exceptionally well-suited for the development of efficient high-power/high-energy lasers and amplifiers operating at approximately 1 μm [4,5], including thin-disk laser configurations [6].

Lutetium aluminum garnet (LuAG), which shares the same crystal structure as YAG [7], possesses notable characteristics. When LuAG crystals are not doped with other elements, they exhibit significant thermal conductivity (κ = 8.3 $Wm^{-1}K^{-1}$), a small coefficient of thermal expansion (CTE = 6.1 × 10^{-6} K^{-1}), and a positive thermo-optic coefficient (dn/dT = 8.3 × 10^{-6} K^{-1}) at room temperature [3]. These properties lead to minimal and positively behaving thermal lensing effects [8].

Interestingly, even though undoped LuAG has lower thermal conductivity compared to YAG, it becomes a more appealing option for incorporating Yb^{3+} ions due to the weak dependency on concentration. This is due to the closer ionic radii and atomic weights of the host material and dopant ions [9–11]. In contrast, YAG experiences a rapid decline in thermal conductivity upon the introduction of Yb^{3+} ions (it is reduced by half when 10 at.% Yb is added), whereas LuAG undergoes only a minor change. Additionally, Yb^{3+} ions in LuAG also have slightly broader absorption characteristics around 940 nm and higher stimulated-emission cross-sections at approximately 1030 nm compared to Yb: YAG [11,12].

In a similar way, LuAG exhibits a comparable pattern to other Yb^{3+}-doped laser host crystals based on lutetium, such as Lu_2O_3 [13], $LuAlO_3$ [14], $LiLuF_4$ [15], and others. Prior studies have documented the successful development of efficient and scalable Yb:LuAG lasers that utilize InGaAs laser diodes as their pump sources, including thin-disk laser configurations [9,16]. The growth process, thermal properties, spectroscopic characteristics, and laser performance of Yb:LuAG crystals have already been detailed in previous literature [7]. It's worth noting that Yb^{3+}-doped LuAG can also be produced using transparent ceramic technology [10,17], enabling efficient laser operation with ceramics [11,18].

The crystal growth of LuAG crystals faces two main obstacles: (i) the expensive Lu_2O_3 raw materials and (ii) the relatively high melting point (2010 °C) [19]. These obstacles can be bypassed by using compositionally "mixed" crystals $(Y_{1-x}Lu_x)_3Al_5O_{12}$, or shortly (Y, Lu) AG. These crystals share the same structure for any value of $0 < x < 1$. Hence, it is worthwhile to investigate Yb^{3+}-doped (Y,Lu)AG crystals as potential materials for generating laser at ~1 μm wavelength. There are some studies on Yb^{3+}-doped "mixed" (Y,Lu)AG ceramics [20,21] but not much on the corresponding crystals. Cheng et al. and R.F. Tian et al. reported on the crystal growth and a few details on the spectroscopy of mixed $Yb:(YLu)_3Al_5O1_2$ crystal samples [22,23]. Lv et al. utilized such crystals in diode-pumped lasers [24]. In this paper, we aimed to explore the structure, vibronic, detailed spectroscopic study, and lasing features of a composition of the mixed yttrium–lutetium aluminum garnet crystal, $(Y_{0.601}Lu_{0.233}Yb_{0.166})_3Al_5O_{12}$.

2. Experimental Section

2.1. Crystal Growth

The Czochralski method, using radio-frequency induction heating, was employed to grow a single crystal of ytterbium-doped mixed yttrium–lutetium aluminum garnet. The raw materials used, including high-purity Yb_2O_3, Lu_2O_3, Y_2O_3, and Al_2O_3 (all with 5N purity), were accurately measured according to the formula $(Y_{0.638}Lu_{0.212}Yb_{0.150})_3Al_5O_{12}$. The crystal growth took place using an oriented [111] seed obtained from an undoped YAG crystal within an atmosphere of argon.

After the growth process, the crystal was gradually cooled to room temperature. To eliminate residual stresses and color centers formed during growth in oxygen-deficient conditions, the as-grown crystal underwent annealing in air at 1400 °C for 12 h. Figure 1a

displays a photograph of the as-grown crystal boule, showcasing its cylindrical shape, which is characteristic of Czochralski-grown garnet crystals (with a diameter of 40 mm and a cylindrical length of 120 mm). The bluish tint of the as-grown crystal is attributed to the presence of color centers (explained below), while the annealed crystal samples are transparent and colorless.

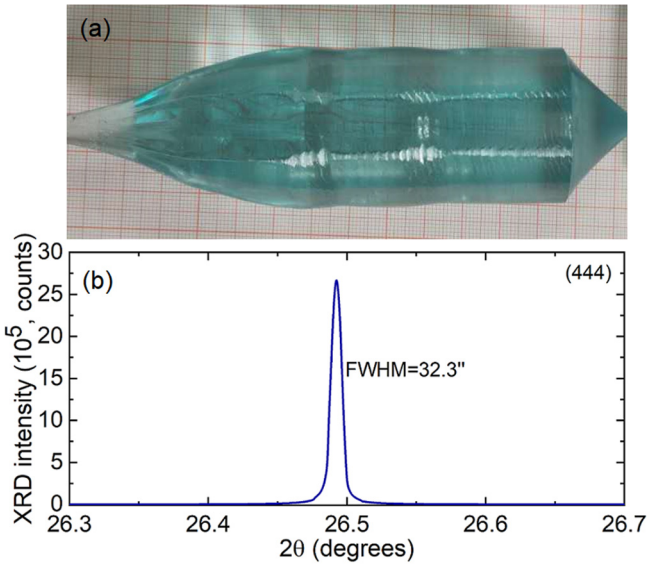

Figure 1. (**a**) A photograph of an as-grown Yb:(Y,Lu)AG crystal. The growth is along the [111] direction; (**b**) the X-ray rocking curve of this crystal, the (444) Bragg reflection.

The quality of the single crystal was evaluated by measuring the X-ray rocking curve using a high-resolution diffractometer (Bruker D8 DISCOVER) with CuKα1 radiation (λ = 1.5406 Å), as depicted in Figure 1b. This measurement was conducted around the (444) reflection, revealing a symmetric profile with a full width at half maximum of 32.3 arcsec. This indicates that the crystal possesses excellent quality and a high degree of crystallinity.

To determine the precise concentrations of Yb^{3+} and Lu^{3+} ions in the grown crystal, we employed Inductively Coupled Plasma-Atomic Emission Spectrometry (ICP-AES). Table 1 compares the starting and actual compositions of the crystal. The actual doping levels of Yb^{3+} and Lu^{3+} are found to be 16.6 at.% and 23.3 at.%, respectively, resulting in corresponding segregation coefficients, $K = C_{crystal}/C_{melt}$, of 1.11 and 1.10, respectively. These values are consistent with prior research [22,25]. The stoichiometry of the grown crystal is determined to be $(Y_{0.601}Lu_{0.233}Yb_{0.166})_3Al_5O_{12}$.

Table 1. Composition of the Yb^{3+}-doped (Y,Lu)AG crystal according to the ICP-MS analysis.

Parameter	Lu^{3+} Content, at.%	Yb^{3+} Content, at.%	Stoichiometry
Melt	21.2	15.0	$(Y_{0.638}Lu_{0.212}Yb_{0.150})_3Al_5O_{12}$
Crystal	23.3	16.6	$(Y_{0.601}Lu_{0.233}Yb_{0.166})_3Al_5O_{12}$
K_{RE}	1.10	1.11	-

2.2. Characterization Methods

The grown crystal's structure and phase purity were examined through X-ray powder diffraction (XRD). This involved using a Bruker-AXS D8-Advance diffractometer (Billerica, MA, USA) with a vertical θ-θ goniometer and Cu Kα1 radiation. A PSD detector LynxEye-XE-T was utilized with an opening angle of 2.94°. The XRD patterns were obtained for Rietveld refinement, employing a step size of 0.02° and a step time of 2 s in the 2θ range spanning from 5° to 80°. The sample was supported on Si (510) to ensure a low background signal.

For acquiring room temperature Raman spectra, a confocal microscope (inVia, Renishaw, Wotton-under-Edge, UK) equipped with a 50 objective (Leica, Wetzlar, Germany) and an Ar^+ ion laser (488.0 nm) was used. Transmission spectra were captured using a spectrophotometer (Lambda 1050, Perkin Elmer, Waltham, MA, USA) and an FTIR spectrometer (Bruker Tensor 27). The emission spectrum was recorded employing a Ti:Sapphire laser as an excitation source and an optical spectrum analyzer (OSA (Yokogawa Electric Corporation, Tokyo, Japan), Ando AQ6315-E). Luminescence decay was investigated in finely powdered crystalline samples using a nanosecond optical parametric oscillator (Horizon, Continuum, Newark, NJ, USA), a 1/4 m monochromator (Oriel 77200), an InGaAs detector, and an 8 GHz digital oscilloscope (DSA70804B, Tektronix, Beaverton, OR, USA). For spectroscopic measurements at low temperatures (12 K), the crystal was positioned on an APD DE-202 closed-cycle cryocooler equipped with an APD HC 2 Helium cryo-compressor and a Lakeshore 330 temperature regulator.

2.3. Laser Characterization

2.3.1. Laser Set-Up Using Ti:Sapphire Laser

The laser setup is depicted in Figure 2. To conduct laser experiments, a rectangular active component was sectioned from the annealed Yb:(Y,Lu)AG crystal along the [111] crystallographic orientation. It had a thickness of 2.03 mm and an aperture measuring 4.0×4.0 mm^2. Both its entrance and exit surfaces were finely polished for laser-grade quality and were left uncoated. This component was affixed onto a passively cooled copper holder using silver paint to enhance heat dissipation. The laser cavity, nearly hemispherical in shape, was constructed with a planar pump mirror (PM) coated for high transmission (HT) at 0.88–0.99 μm and for high reflection (HR, R > 99.9%) at 1.02–1.20 μm. It also incorporated a series of concave output couplers (OC), all with the same radius of curvature (RoC) of −100 mm and a transmission T_{OC} ranging from 1% to 20% at 1.0–1.1 μm. The crystal was positioned at normal incidence in close proximity to the PM with a minimal gap of less than 1 mm. The cavity's physical length was nearly 98 mm.

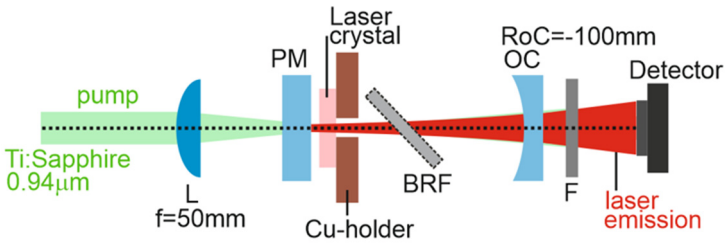

Figure 2. Scheme of the Yb:(Y,Lu)AG laser: L—focusing lens, PM—pump mirror, OC—output coupler, BRF—birefringent plate, F—cut-on filter.

A continuous-wave Ti:sapphire laser (3900S, Spectra Physics) was utilized as the pump source, tuned to 941.0 nm and operating in the fundamental transverse mode (with beam quality factor M^2 near to 1). The pump beam was directed into the laser crystal through the planar pump mirror (PM) using an uncoated spherical CaF2 lens with a focal length (f) of 50 mm, resulting in a pump spot size (2_{wP}) of 34 ± 5 μm. The pumping occurred in a single pass, with the crystal absorbing approximately 97% of the pump radiation (excluding Fresnel losses). Any remaining pump radiation after passing through the output coupler (OC) was filtered out using a long-pass filter (FEL1000, Thorlabs, Newton, NJ, USA). The measured powers were adjusted to account for the transmission of this filter.

For wavelength tuning, an uncoated quartz birefringent disc (BIR1020, New light Photonics, Toronto, ON, Canada) with a diameter of 1 inch and a width of 2.0 mm was selected. It was cut along the a-axis, ensuring that the optical axis lay within the plane of the plate. This disc was positioned at Brewster's angle adjacent to the laser crystal, allowing for control of the laser's vertical polarization. Laser emission spectra were recorded using the same optical spectrum analyzer (OSA) device (Ando AQ6315-E).

2.3.2. Power Scaling Using Diode Pumping

For power scaling, we examined the performance of the diode-pumped laser within a simple plane–plane laser cavity configuration (microchip), as depicted in Figure 3. This configuration was feasible due to the positive thermal lens properties of (Y,Lu)YAG crystals. The same sample that had been employed in the earlier laser experiment using Ti:sapphire laser pumping was used again, this time within the compact microchip cavity. To enhance thermal contact, the crystal was enveloped with indium foil on all four sides and securely mounted in a water-cooled copper holder maintained at approximately 12 °C. The microchip laser cavity was comprised of a flat pump mirror with anti-reflective (AR) coating for the 0.9–1.0 µm range and high reflection (HR) coating for the 1.02–1.20 µm range. It also included a series of flat output couplers with transmission values of 1%, 3%, 5%, or 10% at the laser wavelength. The output coupler (OC) was positioned close to the crystal surface, maintaining an air gap of 300 µm.

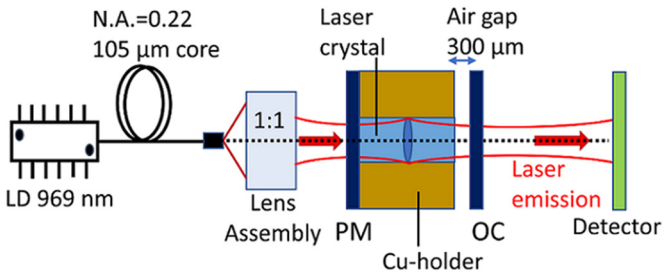

Figure 3. Scheme of the Yb:(Y,Lu)AG microchip laser: LD—laser diode, PM—pump mirror, OC—output coupler.

A fiber-coupled InGaAs laser diode (LD) was employed as the pump source, with a core diameter of 105 µm and a numerical aperture (N.A.) of 0.22. This LD was stabilized using a Volume Bragg Grating (VBG), and its emission exhibited a Full Width at Half Maximum (FWHM) of approximately 0.1 nm, centered at 969.2 ± 0.1 nm. The LD's emission wavelength was kept stable by controlling the temperature with circulating water. The pump beam was focused into the crystal through the planar pump mirror (PM) using an anti-reflection (AR) coated lens assembly, which provided a re-imaging ratio of 1:1 and had a focal length (f) of 30 mm. The focused pump spot size was 2_{wP} = 100 ± 10 µm, with a confocal parameter of 2_{zR} = 3.2 mm. The crystal was pumped in a single-pass configuration, and the total (single-pass) pump absorption was calculated through pump-transmission measurements under non-lasing conditions at the threshold pump power, resulting in an absorption of 97%. The laser output was separated from the remaining pump radiation using a long-pass filter (FEL1000, Thorlabs) with a cutoff wavelength of 1000 nm, exhibiting a transmission of about 84% at 1030 nm. Laser emission spectra were recorded using an Ocean Optics compact spectrometer (model USB 2000+) with a spectral resolution of 0.3 nm.

3. Results and Discussion

3.1. Crystal Structure

The X-ray powder diffraction pattern of the $(Y_{0.601}Lu_{0.233}Yb_{0.166})_3Al_5O_{12}$ crystal, measured at room temperature, is presented in Figure 4a. All identified diffraction peaks match the standard cubic $Y_3Al_5O_{12}$ phase (Crystallography Open Database (COD) card No. 2003066), as shown in Figure 4b. This alignment indicates that the introduction of Yb^{3+} and Lu^{3+} ions does not alter the crystal structure or introduce secondary phases. The measured XRD pattern reveals a cubic garnet structure, with the most prominent diffraction peak observed at 2θ = 33.43°, attributed to the (420) Bragg reflection.

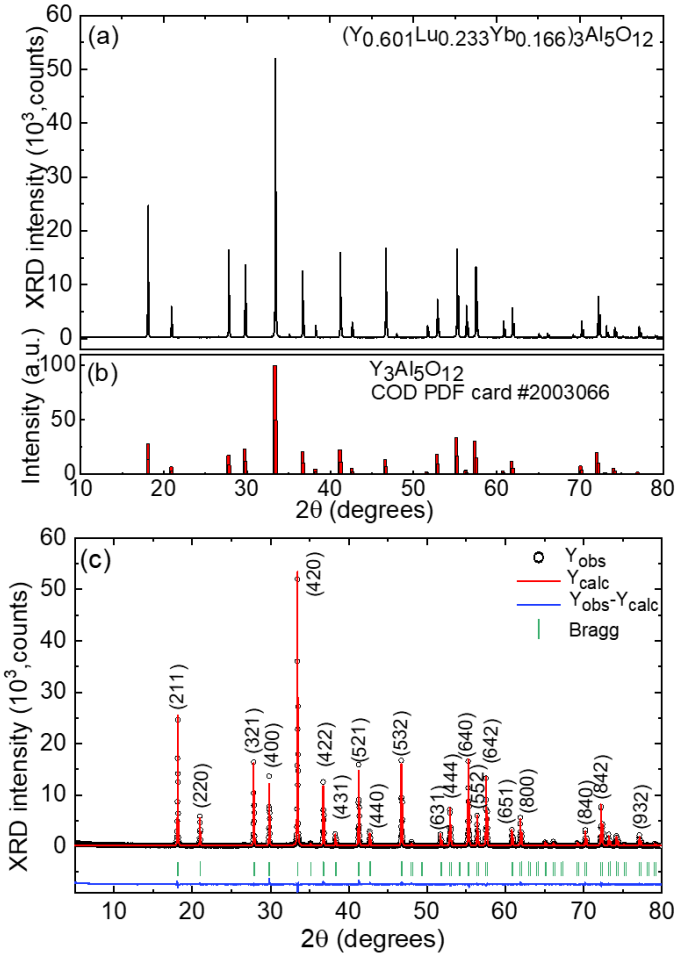

Figure 4. (**a**) Room-temperature X-ray powder diffraction (XRD) pattern of the $(Y_{0.601}Lu_{0.233}Yb_{0.166})_3Al_5O_{12}$ crystal; (**b**) the reference pattern of $Y_3Al_5O_{12}$ garnet (PDF card #2003066, COD database); (**c**) the Rietveld refinement plots (the observed, Y_{obs}, calculated, Y_{calc}, and residual, Y_{obs}-Y_{calc}, profiles); *vertical dashes*—Bragg reflections; *numbers* indicate the Miller's indices (*hkl*).

Table 2 and Figure 4c provide the results of the Rietveld refinement, including the observed (Y_{obs}), calculated (Y_{calc}), and residual (Y_{obs}-Y_{calc}) profiles, along with the Bragg reflections. The $(Y_{0.601}Lu_{0.233}Yb_{0.166})_3Al_5O_{12}$ crystal falls into the cubic class (space group $Ia\bar{3}d$ – O10h, No. 230), with a lattice parameter of a = 11.9790(0) Å (with eight formula units per unit cell), unit cell volume V = 1718.944(0) Å^3, and a calculated crystal density ρ_{calc} = 6.869 g/cm^3. The reliability factors include R_p = 6.07%, R_{wp} = 7.95%, R_{exp} = 3.83%, and the chi-squared value $\chi^2 = (R_{wp}/R_{exp})^2$ is 4.31, indicating a successful fit convergence.

The lattice constant of the grown crystal is slightly smaller than that of undoped $Y_3Al_5O_{12}$ (a = 12.010 Å), primarily due to the smaller ionic radii of both Yb^{3+} (R_{Yb} = 0.858 Å) and Lu^{3+} (R_{Lu} = 0.850 Å) cations compared to the host-forming Y^{3+} ions (R_Y = 0.893 Å). All these values pertain to VIII-fold oxygen coordination. Table 3 provides details on the calculated fractional atomic positions, site occupancy factors (based on ICP-MS analysis results), and isotropic displacement parameters for the $(Y_{0.601}Lu_{0.233}Yb_{0.166})_3Al_5O_{12}$ crystal.

Table 2. Crystallographic data and Rietveld refinement details for the $(Y_{0.601}Lu_{0.233}Yb_{0.166})_3Al_5O_{12}$ crystal.

Parameter	Value
Crystal system	cubic
Space group (IT number, Z)	$Ia\bar{3}d$–O^{10}_h (No. 230, Z = 8)
Hall symbol	-I 4bd 2c 3
Laue class	m-3m
Reduced number of S.O.	24
General multiplicity	96
Calculated density (g/cm^3)	6.869
Lattice constants: $a = b = c$ (Å)	11.9790(0)
$\alpha = \beta = \gamma$ (deg.)	90
Unit-cell volume ($Å^3$)	1718.944(0)
2θ range (deg.)	5–80
2θ step	0.02
Radiation	Cu Kα1 (λ = 1.5418 Å)
No. of reflections	100
Refinement software	Match!-version 3.0 software
Reliability factors	R_p = 6.07%, R_{wp} = 7.95%, R_{exp} = 3.83% and χ^2 = 4.31

Table 3. Fractional atomic coordinates (x/a, y/b, and z/c), site occupancy factors (O.F.), and isotropic displacement parameters (B_{iso}) for the $(Y_{0.601}Lu_{0.233}Yb_{0.166})_3Al_5O_{12}$ crystal.

Atoms	Sites	*x/a*	*y/b*	*z/c*	*O.F.*	B_{iso}, $Å^2$
Y	24*c*	1/8	0	1/4	0.601	1.112(0)
Lu	24*c*	1/8	0	1/4	0.233	1.112(0)
Yb	24*c*	1/8	0	1/4	0.166	1.112(0)
Al1	16*a*	0	0	0	1	1.131(2)
Al2	24*d*	0.3750(0)	0	1/4	1	1.636(8)
O	96*h*	−0.0323(7)	0.0541(3)	0.1521(7)	1	2.011(1)

Figure 5a illustrates a graphical representation of a portion of the Yb:(Y,Lu)AG crystal structure. Within this structure, there is a single type of rare-earth (RE = Y | Lu | Yb) site (Wyckoff: 24c) and two aluminum (Al) sites (16a and 24d). The Al1 atom exhibits coordination with six oxygen atoms, forming [Al1O_6] octahedra. On the other hand, the Al2 atom is coordinated by four oxygen atoms, giving rise to [Al2O_4] tetrahedra. The Yb:(Y,Lu)AG structure is characterized by the presence of vertex-sharing [AlO_6] octahedra and [AlO4] tetrahedra, with metal-to-oxygen (Al–O) bond lengths measured at 1.9732(8) Å (×6) and 1.7390(4) Å (×4), respectively. The rare-earth (RE) atoms exhibit coordination with eight oxygen atoms, forming a distorted [Y | Lu | YbO_8] cube. In this configuration, there are four shorter (2.3127(7) Å) and four longer (2.4003(8) Å) metal-to-oxygen (RE–O) distances. Each set of three [Lu | Y | YbO_8] polyhedra is interconnected by sharing a common O–O edge, as illustrated in Figure 5b, thereby creating a [(Lu | Y | Yb)$_3O_{18}$] group. Each [(Lu | Y | Yb)$_3O_{18}$] group is linked to the [AlO_6] octahedra and [AlO_4] tetrahedra through shared bridges, ensuring the structural integrity and rigidity of the crystal.

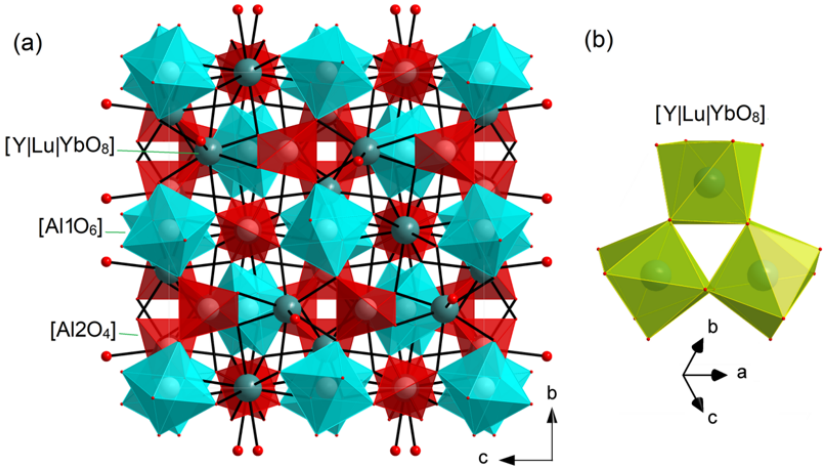

Figure 5. (**a**) A fragment of the crystal structure of Yb:(Y,Lu)AG garnet and projection on the b–c plane; (**b**) connection between the [Y | Lu | YbO_8] polyhedra.

The unpolarized Raman spectra of the as-grown and annealed Yb:(Y,Lu)AG crystals are shown in Figure 6. There are 80 atoms inside the unit-cell of O^{10}_h cubic garnets. Following factor-group analysis, it leads to 97 lattice modes. At the center of the Brillouin zone ($\boldsymbol{k}$ = 0), the irreducible representations can be written as follows: $\Gamma = 3A_{1g} + 8E_g + 14F_{2g} + 5A_{1u} + 5A_{2u} = 5A_{2g} + 10E_u + 14F_{1g} + 16F_{2u} + 17F_{1u}$, among which 25 modes ($A_{1g}$, E_g and F_{2g}) are Raman-active [26]. In the spectra, 19 modes are observed. The most intense Raman band at 786 cm^{-1} (A_{1g}) is assigned to the breathing mode of the [AlO_4] tetrahedrons [27]. The maximum phonon energy of Yb:(Y,Lu)AG is 860 cm^{-1}.

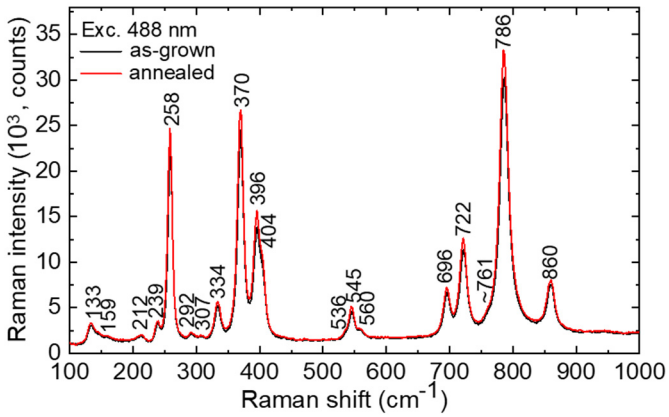

Figure 6. RT unpolarized Raman spectra of the as-grown and annealed Yb:(Y,Lu)AG crystals; λ_{exc} = 488 nm; *numbers* indicate the Raman frequencies in cm^{-1}.

3.2. Optical Spectroscopy

Figure 7a,b display the transmission spectra of laser-grade-polished samples of Yb:(Y,Lu)AG, each with a thickness of 2.0 mm, obtained from both as-grown and annealed crystals. In the visible spectrum, the as-grown crystal exhibits several broad absorption bands, with centers around ~0.28, 0.37, and 0.62 µm, contributing to its slight bluish coloration. These absorption bands are well-documented for Yb-doped garnets produced under inert atmospheric conditions [28]. They are primarily linked to the presence of oxygen vacancies and Yb^{2+} ions that arise in oxygen-deficient conditions. Annealing the crystal in oxygen-rich conditions promotes the conversion of Yb^{2+} to Yb^{3+}, causing these bands to disappear and improving the crystal's transparency. Indeed, the transmission spectrum of the annealed crystal lacks these bands, although a weak band centered at ~0.26 µm emerges. The

position of the UV absorption edge was determined by analyzing the Tauc plot [29] for direct allowed transitions (based on the electronic structure of YAG [30]), involving plotting $(\alpha_{abs} \times h\nu)^{1/2}$ against photon energy $h\nu$ (where α_{abs} is the absorption coefficient). This analysis revealed the UV absorption edge at λ_{UV} = 0.244 µm, corresponding to an optical bandgap energy Eg of 5.08 eV (as shown in the inset in Figure 7a). The optical curve displays both linear and nonlinear segments, representing distinct features of permissible transitions. The linear part of the curve, predominantly found on the higher energy side of the Tauc plot, signifies the primary absorption of the materials. Conversely, the nonlinear segment, which is located at energy < Eg, corresponds to residual absorption associated with defect states [31,32]. Moving into the infrared (IR) range, the Yb:(Y,Lu)AG crystals maintain transparency until λ_{IR} = 6.1 µm, as depicted in Figure 7b. The IR transmission edge corresponds to an energy of 2 × 786 cm^{-1} (indicative of two-phonon absorption, as described in the Raman spectra earlier). It is worth noting that crystal annealing has a limited impact on the IR transmission spectra.

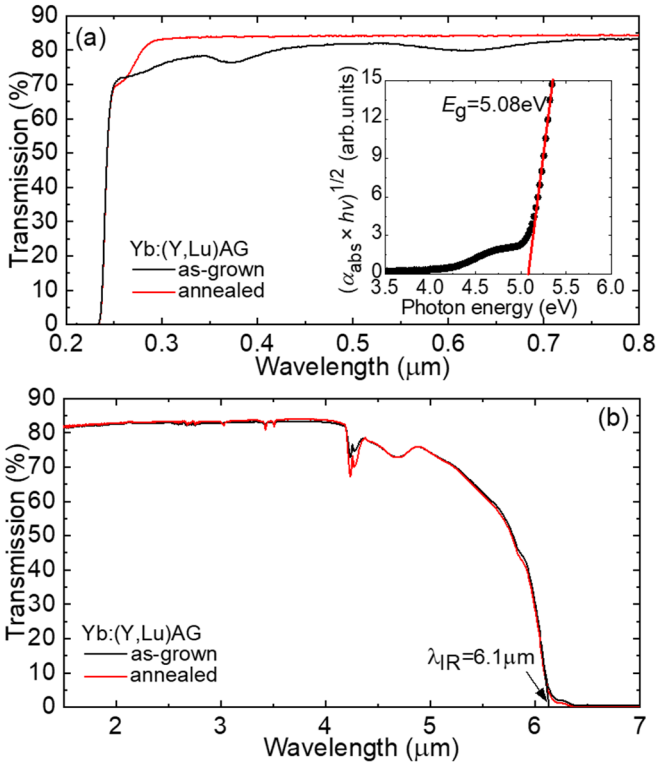

Figure 7. Transmission spectra of the as-grown and annealed Yb:(Y,Lu)AG crystals: (**a**) the spectral range of 0.2–0.8 µm; *inset*—Tauc plot for evaluating the optical bandgap E_g; (**b**) the spectral range of 1.5–7 µm. Sample thickness: t = 2.03 mm.

In Figure 8a, we present the absorption spectrum of the annealed Yb:(Y,Lu)AG crystal at room temperature (293 K). The absorption observed around 1 µm arises from the $^2F_{7/2} \rightarrow {}^2F_{5/2}$ transition of Yb^{3+} ions. The peak absorption cross-section σ_{abs}, which is calculated as α_{abs}/N_{Yb}, is measured at 0.80 × 10^{-20} cm^2 at 969.2 nm. This corresponds to the "zero phonon line" (ZPL) transition occurring between the weakest Stark sublevels within the relevant multiplets. Notably, the bandwidth (expressed as the full width at half maximum, FWHM) of the ZPL in absorption, denoted as $\Delta\lambda_{abs}$, is relatively narrow, measuring less than 3 nm. Furthermore, at shorter wavelengths, another prominent absorption line (σ_{abs} = 0.78 × 10^{-20} cm^2) is observed, centered at 941.0 nm, with a much broader bandwidth $\Delta\lambda_{abs}$ of approximately 19 nm. This line holds greater promise for pumping Yb:(Y,Lu)AG crystals using diode lasers based on InGaAs, as its wider bandwidth has the potential to mitigate the impact of temperature-related wavelength drift in these diode lasers.

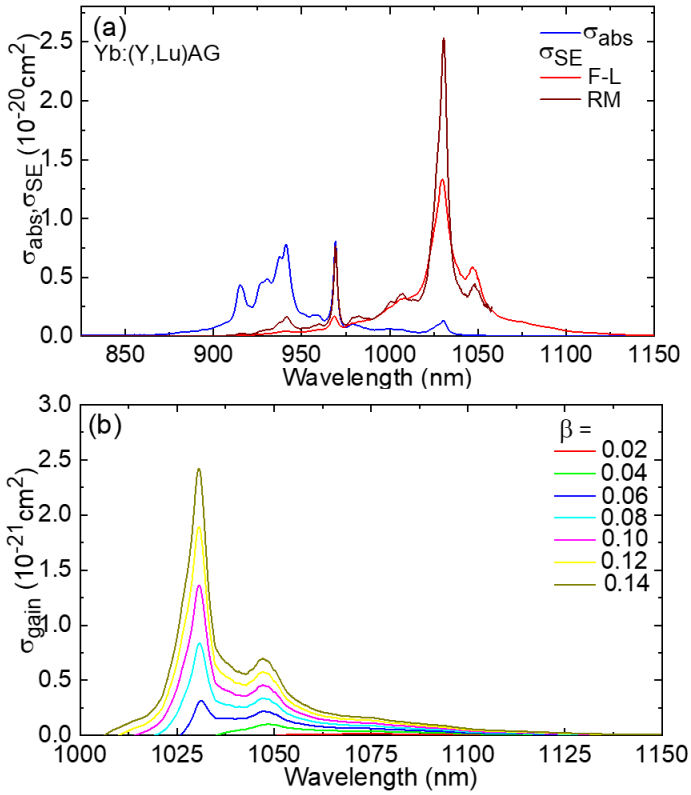

Figure 8. Transition cross-sections of Yb^{3+} ions (the $^2F_{7/2} \longleftrightarrow {}^2F_{5/2}$ transition) in the Yb:(Y,Lu)AG crystal: (**a**) absorption, σ_{abs}, and stimulated-emission (SE), σ_{SE}, cross-sections; F-L: Füchtbauer–Ladenburg equation; RM: reciprocity method; (**b**) gain cross-sections, $\sigma_{gain} = \beta\sigma_{SE} - (1 - \beta)\sigma_{abs}$, β—inversion ratio.

The stimulated-emission (SE) cross-section, denoted as σ_{SE}, was determined through two different calculation methods. The first method relies on the Füchtbauer–Ladenburg (F-L) formula [33]:

$$\sigma_{SE}(\lambda) = \frac{\lambda^5}{8\pi < n >^2 \tau_{rad} c} \frac{W\prime(\lambda)}{\int \lambda W\prime(\lambda) d\lambda}, \quad (1)$$

In this equation, λ represents the wavelength of light, and <n> is the refractive index of the host material, which is approximately 1.819 and corresponds to the mean emission wavelength (derived from refractive index values for YAG [34] and LuAG [19]). τ_{rad} signifies the radiative lifetime of the emitting state, specifically the $^2F_{5/2}$ state of Yb^{3+} ions. The constant "c" denotes the speed of light, and $W'(\lambda)$ refers to the luminescence spectrum that has been adjusted to account for the response of the experimental setup.

The second approach uses the reciprocity method (RM) [35]:

$$\sigma_{SE}(\lambda) = \sigma_{abs}(\lambda) \frac{Z_1}{Z_2} \exp\left(-\frac{hc/\lambda - E_{ZPL}}{kT}\right), \quad (2)$$

Here, h represents the Planck constant, k stands for the Boltzmann constant, T signifies the temperature (room temperature, RT), E_{ZPL} denotes the energy associated with the ZPL transition, and Z_m pertains to the partition coefficients of the lower (m = 1, $^2F_{7/2}$) and upper (m = 2, $^2F_{5/2}$) multiplets of the Yb^{3+} ion:

$$Z_m = \sum_k g_k^m \exp(-E_k^m/kT). \quad (3)$$

where $g^m{}_k = 1$ represents the degeneracy of the Stark sublevel with the index k, and it is based on the energy $E^m{}_k$ calculated from the lowest sublevel within each multiplet.

By simultaneously applying the F–L formula and RM, we can obtain a comprehensive spectrum of the SE cross-section. This approach serves a dual purpose: it helps mitigate the influence of reabsorption on observed luminescence spectra, which can be particularly significant in heavily Yb^{3+}-doped crystals, and it accounts for the impact of extremely low absorption values measured at very long wavelengths. The outcomes regarding σ_{SE} are depicted in Figure 8a. The spectra derived from both methods show reasonable agreement with each other. In the spectral range where laser operation is anticipated (above the ZPL in emission), the maximum σ_{SE} is measured at 2.53×10^{-20} cm^2 at 1031 nm, with the corresponding emission bandwidth (FWHM) $\Delta\lambda_{em}$ spanning approximately 8 nm. Notably, there is a good correspondence between the σSE spectra calculated using the F–L formula and RM when considering the radiative lifetime of the upper multiplet, which is $\tau_{rad} = 1.00 \pm 0.05$ ms.

In the case of Yb^{3+} ions, which operate under a quasi-three-level laser scheme with reabsorption, the gain cross-sections, denoted as σgain, are typically calculated to determine the anticipated laser wavelength and the extent of the gain bandwidth. In this context, $\sigma_{gain} = \beta\sigma_{SE} - (1 - \beta)\sigma_{abs}$, where $\beta = N^2(^2F_{5/2})/N_{Yb}$ represents the inversion ratio and N^2 signifies the population of the upper laser level. The gain profiles for the Yb:(Y,Lu)AG crystal are depicted in Figure 8b. As the inversion ratio increases, the peak in the gain spectra shifts from 1048 nm (for low $\beta < 0.05$) to 1030 nm (for higher β). When $\beta = 0.10$, the gain bandwidth of the latter peak (FWHM) measures approximately 7 nm.

Figure 9 illustrates the luminescence lifetime curve for Yb^{3+} ions. To minimize the influence of reabsorption, also known as radiation trapping, on the measured luminescence lifetime (τ_{lum}), we conducted the decay analysis using finely powdered crystalline samples. The resulting decay curve fits well to a single exponential model, yielding a luminescence lifetime of τ_{lum} equal to 1.063 ms. It is noteworthy that for the bulk sample, a significantly longer lifetime of 1.554 ms is observed. This measured luminescence lifetime, unaffected by reabsorption, closely aligns with the radiative lifetime estimate obtained from the calculation of the SE cross-sections, as mentioned earlier.

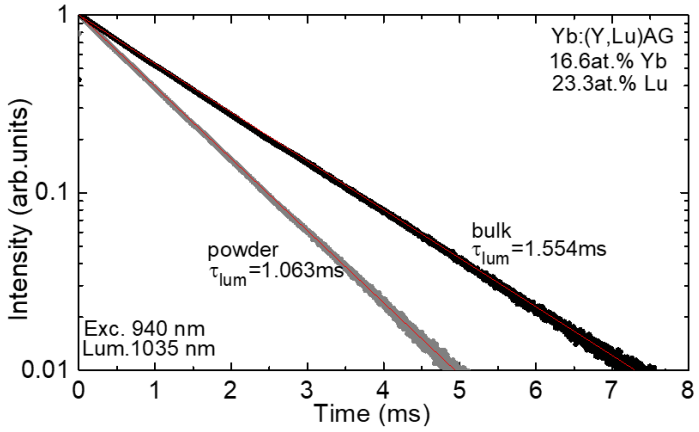

Figure 9. RT luminescence decay curve of Yb^{3+} ions in the annealed Yb:(Y,Lu)AG crystal (bulk and powdered crystalline samples); λ_{exc} = 940 nm; λ_{lum} = 1035 nm.

In Figure 10a,b, we present the absorption and luminescence spectra of Yb^{3+} ions in the (Y,Lu)AG crystal measured at a low temperature of 12K. The absorption spectrum is plotted against photon energy ($h\nu_{ph}$), while the emission spectrum is plotted against ($E_{ZPL} - h\nu_{ph}$) to facilitate the determination of the Stark sublevel energies within the Yb^{3+} multiplets. In the crystal field of (Y,Lu)AG, Yb^{3+} ions are anticipated to replace the host-forming Y^{3+} | Lu^{3+} cations, occupying a specific site with D_2 symmetry and VIII-fold coordination by oxygen. Within each $^{2S+1}L_J$ multiplet of Yb^{3+} ions, the crystal field splits the states into J + 1/2 components, labeled as 0…3 for the ground state and 0′…2′ for the excited state. By analyzing the low-temperature spectra and excluding the phonon

sidebands (as determined from the Raman spectrum), we can assign electronic transitions that occur between the Stark sublevels.

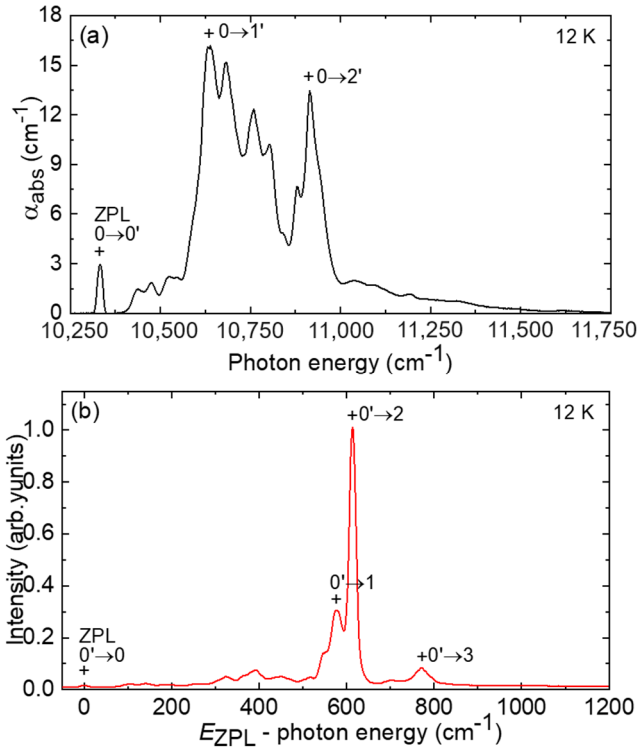

Figure 10. LT (12 K) (**a**) absorption and (**b**) luminescence spectra of Yb^{3+} ions in the annealed Yb:(Y,Lu)AG crystal; "+" indicate the electronic transitions.

Table 4 displays the crystal-field splitting of Yb^{3+} ions within the (Y,Lu)AG crystal, and we have included a comparison with the splitting observed in YAG and LuAG crystals [7]. In the case of Yb:(Y,Lu)AG, the energy associated with the zero-phonon line (ZPL) is measured at E_{ZPL} = 10,333 cm^{-1}, equivalent to a ZPL wavelength of 967.8 nm at 12 K. Notably, the total Stark splitting of the ground state, $\Delta E(^2F_{7/2})$, is relatively substantial, measuring 771 cm^{-1}, and this characteristic is advantageous for achieving low-threshold laser operation. The partition functions are represented as Z1 = 1.130 and Z2 = 1.282, with a ratio of Z1/Z2 equal to 0.881.

Table 4. Experimental Stark splitting of Yb^{3+} multiplets in the (Y,Lu)AG (this work), YAG, and LuAG crystals [7].

Yb^{3+} Multiplet	***E*, cm^{-1}**		
$^{2S+1}L_J$	(Y,Lu)AG	YAG	LuAG
$^2F_{7/2}$	0	0	0
	578	565	602
	613	612	643
	771	785	764
$^2F_{5/2}$	10,333	10,327	10,333
	10,636	10,650	10,643
	10,915	10,923	10,908

To provide insights into laser operation, we have summarized the spectroscopic properties of the Yb:(Y,Lu)AG crystal in Table 5 and compared them to those of the parent crystals, Yb:YAG and Yb:LuAG (as presented in this work).

Table 5. Spectroscopic properties of Yb^{3+} ions in the (Y,Lu)AG, YAG and LuAG crystals.

Crystal	σ_{abs}, 10^{-20} cm^2	λ_{abs}, nm	$\Delta\lambda_{abs}$, nm	σ_{SE}, 10^{-20} cm^2	λ_{em}, nm	τ_{rad}, ms
(Y,Lu)AG	0.80 0.78	969.2 941.0	<3 19	2.53	1030.6	1.00
YAG	0.80 0.77	969.0 ~942	2.5 ~18	2.31	~1030	0.95
LuAG	0.73 0.79	969.0 940.7	<3 ~20	2.76	1030.4	1.01

3.3. Laser Performance

3.3.1. Laser Performance Using Ti:Sapphire Pumping

The performance of the free-running Yb:(Y,Lu)AG laser, pumped at λ_P = 941.0 nm, is illustrated in Figure 11a. The laser achieved a peak output power of 1.04 W, emitting at wavelengths of 1029–1031 nm and 1047–1049 nm. Its slope efficiency η, relative to the absorbed pump power, reached 76.4%, and the laser exhibited a threshold of 76 mW (with T_{OC} = 10%). When the incident pump power reached its maximum at 1.83 W, the optical-to-optical conversion efficiency was 56.8%. As the output coupling (T_{OC}) increased, the laser threshold gradually rose, starting from 39 mW (T_{OC} = 1%) and reaching 80 mW (TOC = 20%). The output characteristics displayed a linear relationship well beyond the laser threshold.

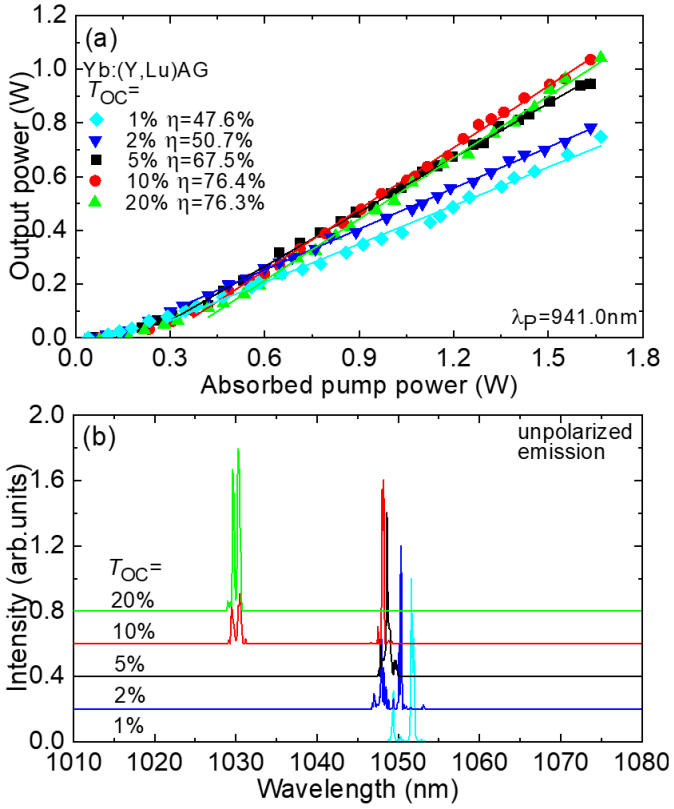

Figure 11. Free-running Yb:(Y,Lu)AG laser: (**a**) input–output dependences, η—slope efficiency; (**b**) typical spectra of laser emission (unpolarized radiation), λ_P = 941.0 nm.

Figure 11b presents typical spectra of the laser emission, which was unpolarized. For lower output coupling (T_{OC} = 1–5%), the laser emitted at 1.05 µm, while for T_{OC} = 10%, it exhibited emission in two spectral ranges, specifically at 1.03 and 1.05 µm. With even higher T_{OC} (T_{OC} = 20%), the laser operated exclusively in the shorter-wavelength range.

This behavior aligns with the gain spectra, taking into consideration the need to increase the inversion within the laser crystal to compensate for higher output coupling losses. This phenomenon can be explained by the quasi-three-level scheme of the Yb^{3+} laser transition from $^2F_{5/2}$ to $^2F_{7/2}$, which involves reabsorption at the laser wavelength. The multi-peak structure observed in the laser emission spectra is attributed to the relatively broad gain spectra of Yb^{3+} ions within the (Y,Lu)AG crystal and etalon (Fabry–Perot) effects occurring at the interfaces of the crystal and the pump mirror (PM). It is important to note that the laser operated in the fundamental transverse mode, with measured beam quality factors at the maximum pump power ($M^2_{x,y}$) being less than 1.1.

The laser's excitation spectrum, which shows how the output power varies with the pump wavelength (λ_P), was also measured, as depicted in Figure 12. To conduct this measurement, the incident pump power on the crystal was maintained at a constant 0.91 W. The shape of the laser excitation curve closely mirrors that of the absorption cross-section spectrum for Yb^{3+}:(Y,Lu)AG. Consequently, laser operation was successfully attained within the range of λP spanning from 899.7 to 985.7 nm. Notably, the two optimal pump wavelengths are 941.0 nm and 969.2 nm, corresponding to the zero-phonon line (ZPL).

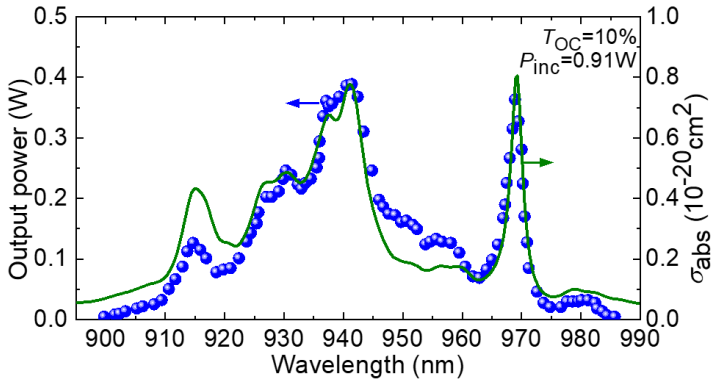

Figure 12. Laser excitation curve for the Yb:(Y,Lu)AG laser: *blue circles*—experimental data on the output power; *green curve*—absorption cross-section; σ_{abs}, spectrum; T_{OC} = 10%; P_{inc} = 0.91 W.

To investigate wavelength tunability, a birefringent plate was inserted into the laser cavity and oriented at Brewster's angle. Employing a 1% output coupler (OC), we achieved continuous wavelength tuning across the range of 1026.4–1078.0 nm, corresponding to a tuning span of 51.6 nm at the zero-power level, as illustrated in Figure 13. The highest output power was achieved at approximately 1050 nm, aligning with the gain spectra for small β values and the characteristics of the free-running laser spectra.

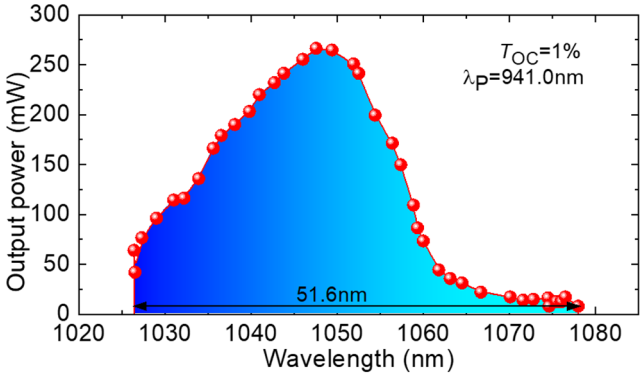

Figure 13. Wavelength tuning curve of the Yb:(Y,Lu)AG laser; T_{OC} = 1%; λ_P = 941.0 nm.

3.3.2. Diode-Pumped Laser Performance

Microchip laser operation has been successfully achieved using the Yb:(Y, Lu)YAG crystal. The input–output characteristics are presented in Figure 14a, illustrating the power scaling achieved with fiber-coupled InGaAs laser diode pumping. The laser generated its maximum output power at 9.10 W, operating at a wavelength of 1050.7 nm, with a slope efficiency η of 76% relative to the absorbed pump power. The laser's threshold power (P_{th}) was measured at 0.82 W (with T_{OC} = 3%). As the output coupling (T_{OC}) increased, the laser threshold gradually rose, ranging from 0.62 W (T_{OC} = 1%) to 1.04 W (T_{OC} = 10%).

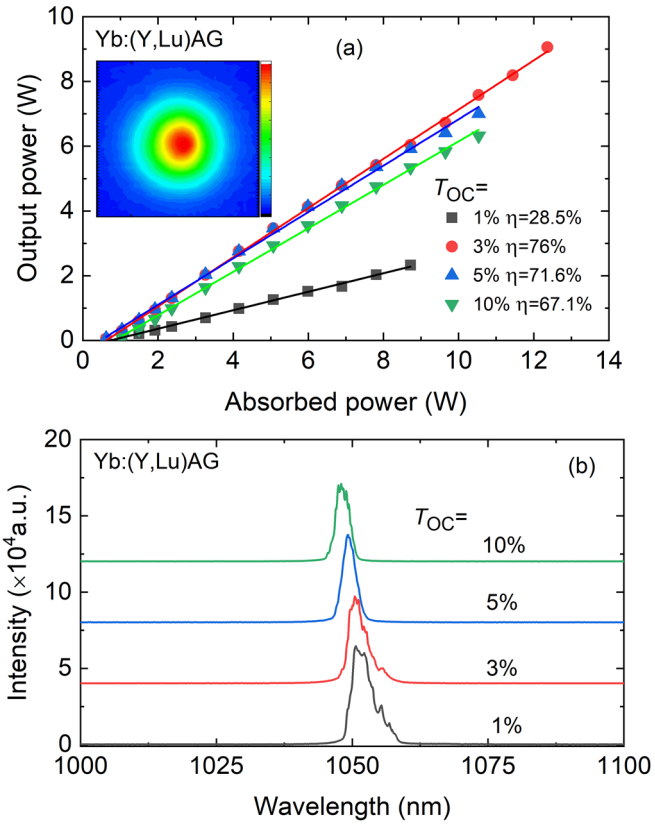

Figure 14. Continuous-wave Yb:(Y,Lu)AG microchip laser: (**a**) input–output dependences, η—slope efficiency; *inset:* 2D spatial intensity profile of the laser output from a CW Yb:(Y, Lu)AG laser measured at P_{abs} = 11.44 W; (**b**) typical laser emission spectra measured at P_{abs} = 5.98 W.

Using this diode for pumping resulted in a lower quantum defect (η_h~6–8%, depending on the OC), ensuring that the input–output characteristics remained linear without experiencing thermal roll-over across the entire range of pump powers studied. This linearity was maintained up to a minimum of 12.36 W of absorbed pump power.

The Yb:(Y,Lu)YAG microchip laser's typical laser emission spectra are depicted in Figure 4. As the output coupling increased from 1% to 10%, there was a noticeable shift towards shorter wavelengths in the emission, transitioning from 1051.3 nm to 1047.8 nm. This wavelength shift can be attributed to the quasi-three-level nature of the Yb^{3+} laser scheme.

In the inset of Figure 14a, the output beam profile of the Yb:(Y,Lu)YAG microchip laser can be observed, which was captured using a near-IR camera positioned 10 cm from the output coupler (T_{OC} = 3%, P_{abs} = 11.44 W). As expected, due to the low astigmatism of the thermal lens, the Yb:(Y, Lu)YAG microchip laser displayed a nearly circular output beam. This outstanding beam profile can also be attributed to the precise mode-matching achieved within the microchip laser cavity.

4. Conclusions

In summary, we present the growth process via the Czochralski method, detailed structural refinement, and an extensive spectroscopic examination of a novel composite, ytterbium-doped yttrium–lutetium aluminum garnet, denoted as $(Y_{0.638}Lu_{0.212}Yb_{0.150})_3Al_5O_{12}$. This crystal possesses a cubic structure (space group $Ia\bar{3}d$, lattice parameter a = 11.9790(0) Å), sharing structural similarity with its parent compound, $Y_3Al_5O_{12}$. It exhibits promising spectroscopic characteristics in terms of Yb^{3+} ion doping, including a broad absorption band around 940 nm, well-matched to InGaAs laser diode emissions. Moreover, it showcases a relatively high stimulated-emission cross-section of 2.53×10^{-20} cm^2 at approximately 1031 nm, along with a substantial reabsorption-free luminescence lifetime of 1.063 ms. Efficient laser operation of this crystal, doped with 16.6 at.% Yb^{3+}, was successfully achieved under high-brightness pumping. This yielded an impressive output power of 1.04 W within the range of 1.03–1.05 μm, demonstrating a high slope efficiency of 76.4% and a low laser threshold of only 76 mW. Additionally, we demonstrated continuous wavelength tuning across 51.6 nm (1026.4–1078.0 nm). Furthermore, through microchip laser operation, we achieved power scaling with a maximum output power of approximately 9 W at around 1.05 μm, exhibiting a slope efficiency of 76%. This "mixed" crystal shows promise for diode-pumped, power-scalable lasers operating at approximately 1 μm.

Author Contributions: Investigation: S.S., P.L. (Pavel Loiko), M.P., P.L. (Pauline Lehoux), Y.W., W.C., R.M.S. and X.M.; Methodology: S.S. and P.L. (Pavel Loiko); Writing & Original Draft: S.S. and P.L. (Pavel Loiko); Review & Editing: P.L. (Pavel Loiko), V.J., M.S., T.M., V.P., R.M.S., P.C. and X.M.; Resources: M.S., T.M., M.A. and F.D.; Conceptualization: M.A., F.D., P.C. and X.M.; Supervision: X.M. All authors have read and agreed to the published version of the manuscript.

Funding: This research has been possible with the support of the Secretaria d'Universitats i Recerca del Departament d'Empresa i Coneixement de la Generalitat de Catalunya, the European Union (EU), the European Social Fund (ESF) (2022 FI_B2 00021), and Grant PID2019-108543RB-I00 of MCIN/AEI/10.13 039/501100011033. This work was co-financed by the European Regional Development Fund and the state budget of the Czech Republic (project HiLASE CoE: Grant No. CZ.02.1.01/0.0/0.0/15_006/0000674) and the EU Horizon 2020 research and innovation programme under Grant No. 739573.

Institutional Review Board Statement: This study did not require ethical approval.

Informed Consent Statement: Not applicable.

Data Availability Statement: The data that support this study are available from the corresponding author upon reasonable request.

Conflicts of Interest: The authors declare no conflict of interest.

References

1. Taira, T.; Tulloch, W.M.; Byer, R.L. Modeling of Quasi-Three-Level Lasers and Operation of Cw Yb:YAG Lasers. *Appl. Opt.* **1997**, *36*, 1867–1874. [CrossRef]
2. Wang, C.A.; Fan, T.Y.; Lacovara, P.; Choi, H.K.; Aggarwal, R.L. Room-Temperature Diode-Pumped Yb:YAG Laser. *Opt. Lett.* **1991**, *16*, 1089–1091.
3. Aggarwal, R.L.; Ripin, D.J.; Ochoa, J.R.; Fan, T.Y. Measurement of Thermo-Optic Properties of $Y_3Al_5O_{12}$, $Lu_3Al_5O_{12}$, $YAlO_3$, $LiYF_4$, $LiLuF_4$, $BaY2F_8$, $KGd(WO_4)_2$, and $KY(WO_4)_2$ Laser Crystals in the 80–300K Temperature Range. *J. Appl. Phys.* **2005**, *98*, 103514. [CrossRef]
4. Paschotta, R.; Schaer, S.F.; der Au, J.A.; Keller, U.; Moser, M.; Hönninger, C. High-Power Diode-Pumped Passively Mode-Locked Yb:YAG Lasers. *Opt. Lett.* **1999**, *24*, 1281–1283.
5. Emanuel, M.A.; Avizonis, P.V.; Monroe, R.S.; Honea, E.C.; Harris, D.G.; Beach, R.J.; Mitchell, S.C.; Payne, S.A.; Skidmore, J.A.; Sutton, S.B. High-Power Dual-Rod Yb:YAG Laser. *Opt. Lett.* **2000**, *25*, 805–807.
6. Innerhofer, E.; Südmeyer, T.; Brunner, F.; Häring, R.; Aschwanden, A.; Paschotta, R.; Hönninger, C.; Kumkar, M.; Keller, U. 60-W Average Power in 810-Fs Pulses from a Thin-Disk Yb:YAG Laser. *Opt. Lett.* **2003**, *28*, 367–369. [CrossRef]
7. Canibano, H.; Ródenas, A.; Jaque, D.; Petrosyan, A.G.; Boulon, G.; Guyot, Y.; Brenier, A.; Eganyan, A. Growth, Spectroscopic, and Laser Properties of Yb^{3+}-Doped $Lu_3Al_5O_{12}$ Garnet Crystal. *JOSA B* **2006**, *23*, 676–683.

8. Veselský, K.; Šulc, J.; Jelínková, H.; Nejezchleb, K.; Škoda, V. Yb Doping Concentration and Temperature Influence on Yb:LuAG Thermal Lensing. In *Solid State Lasers XXV: Technology and Devices*; SPIE: Bellingham, WA, USA, 2016; Volume 9726, pp. 281–286.
9. Fredrich-Thornton, S.T.; Beil, K.; Peters, R.; Tellkamp, F.; Kränkel, C.; Petermann, K.; Huber, G. Thermal and Laser Properties of Yb:LuAG for KW Thin Disk Lasers. *Opt. Express* **2010**, *18*, 20712–20722.
10. Fu, Y.; Li, J.; Wang, C.; Xie, T.; Li, W.; Wu, L.; Pan, Y. Fabrication and Properties of Highly Transparent Yb:LuAG Ceramics. *J. Alloys Compd.* **2016**, *664*, 595–601. [CrossRef]
11. Nakao, H.; Ueda, K.; Shirakawa, A.; Yagi, H.; Yanagitani, T. CW and Mode-Locked Operation of Yb^{3+}-Doped $Lu_3Al_5O_{12}$ Ceramic Laser. *Opt. Express* **2012**, *20*, 15385–15391. [CrossRef]
12. Yu, H.; Xu, J.; Xu, Z.; Xu, X.; Liang, X.; Zhao, Z.; He, J.; Li, J. LD Pumped Yb:LuAG Mode-Locked Laser with 7.63ps Duration. *Opt. Express* **2009**, *17*, 11537–11542.
13. Baer, C.R.E.; Petermann, K.; Marchese, S.V.; Peters, R.; Engqvist, A.G.; Huber, G.; Keller, U.; Golling, M.; Kränkel, C.; Maas, D.J.H.C.; et al. Efficient Femtosecond High Power Yb:Lu2O3 Thin Disk Laser. *Opt. Express* **2007**, *15*, 16966–16971.
14. Kisel, V.; Rudenkov, A.; Petrosyan, A.; Hovhannesyan, K.; Yasukevich, A.; Kuleshov, N. Spectroscopy and Continuous Wave Laser Performance of Yb^{3+}:$LuAlO_3$ Crystal. *Opt. Lett.* **2016**, *41*, 5805–5808.
15. Lin, H.; Tonelli, M.; Pirzio, F.; Agnesi, A.; Volpi, A.; Di Lieto, A.; Cittadino, G. Crystal Growth, Spectroscopic Characterization, and Sub-100 Femtosecond Mode-Locked Operation of a Yb:$LiLuF_4$ Laser. *JOSA B* **2016**, *33*, 2350–2356. [CrossRef]
16. Dong, J.; Ueda, K.; Kaminskii, A.A. Laser-Diode Pumped Efficient Yb:LuAG Microchip Lasers Oscillating at 1030 and 1047 Nm. *Laser Phys. Lett.* **2010**, *7*, 726–733. [CrossRef]
17. Basyrova, L.; Maksimov, R.; Shitov, V.; Baranov, M.; Mikhaylovsky, V.; Khubetsov, A.; Dymshits, O.; Mateos, X.; Loiko, P. Effect of SiO2 Addition on Structural and Optical Properties of Yb:$Lu_3Al_5O_{12}$ Transparent Ceramics Based on Laser Ablated Nanopowders. *J. Alloys Compd.* **2019**, *806*, 717–725. [CrossRef]
18. Basyrova, L.; Loiko, P.; Maksimov, R.; Shitov, V.; Serres, J.M.; Griebner, U.; Petrov, V.; Aguiló, M.; Díaz, F.; Mateos, X. Comparative Study of Yb:$Lu_3Al_5O_{12}$ and Yb:Lu_2O_3 Laser Ceramics Produced from Laser-Ablated Nanopowders. *Ceram. Int.* **2021**, *47*, 6633–6642. [CrossRef]
19. Kuwano, Y.; Suda, K.; Ishizawa, N.; Yamada, T. Crystal Growth and Properties of $(Lu,Y)_3Al_5O_{12}$. *J. Cryst. Growth* **2004**, *260*, 159–165. [CrossRef]
20. Pirri, A.; Toci, G.; Li, J.; Xie, T.; Pan, Y.; Babin, V.; Beitlerova, A.; Nikl, M.; Vannini, M. High Efficiency Laser Action in Mildly Doped Yb:LuYAG Ceramics. *Opt. Mater.* **2017**, *73*, 312–318. [CrossRef]
21. Balashov, V.V.; Zakharov, L.Y.; Inyushkin, A.V.; Kanaev, A.Y.; Kozlov, A.B.; Kozlova, S.M.; Koromyslov, A.L.; Lopukhin, K.V.; Luzanov, V.A.; Pervakov, K.S.; et al. Comparative Study of $Lu_xY_{1-x}AG$ (x = 0..1) Laser Ceramics Doped with 5% Yb^{3+}. *Ceram. Int.* **2022**, *48*, 6294–6301. [CrossRef]
22. Tian, R.; Tian, R.; Pan, M.; Zhang, L.; Zhang, L.; Qi, H. Crystal Growth and Spectral Properties of $(Yb_{0.15}Lu_{0.85x}Y_{0.85-0.85x})_3Al_5O_{12}$ Single Crystals. *Chin. Opt. Lett.* **2022**, *20*, 121601. [CrossRef]
23. Cheng, S.; Xu, X.; Li, D.; Zhou, D.; Wu, F.; Zhao, Z.; Xu, J. Growth and Spectroscopic Properties of Yb:$Lu_{1.5}Y_{1.5}Al_5O_{12}$ Mixed Crystal. *Opt. Mater.* **2010**, *33*, 112–115. [CrossRef]
24. Lv, S.; Gao, C.; Tian, Z.; Su, X.; Wang, G.; Zhu, G.; Wang, B.; Kumar, S.; Xu, X.; Yu, H.; et al. Diode-Pumped Continuous-Wave Dual-Wavelength and Q-Switched Yb:LuYAG Lasers. *Opt. Commun.* **2021**, *478*, 126356. [CrossRef]
25. Shim, J.B.; Yoshikawa, A.; Nikl, M.; Pejchal, J.; Yoon, D.H.; Isshiki, M.; Fukuda, T. Growth and Characterization of Yb^{3+}-Doped $(Lu,Y)AlO_3$ Fiber Single Crystals Grown by the Micro-Pulling-down Method. *Jpn. J. Appl. Phys. Part. 1 Regul. Pap. Short. Notes Rev. Pap.* **2004**, *43*, 7661–7664. [CrossRef]
26. Kaminskii, A.A.; Rhee, H.; Lux, O.; Eichler, H.J.; Bagayev, S.N.; Yagi, H.; Ueda, K.; Shirakawa, A.; Dong, J. Stimulated Raman Scattering in "Garnet" $Lu_3Al_5O_{12}$ Ceramics—A Novel Host-Materiel for Ln- and TM-Lasant Ions. *Laser Phys. Lett.* **2011**, *8*, 458–464. [CrossRef]
27. Papagelis, K.; Ves, S. Infrared Spectroscopy and Lattice Dynamical Calculations of $Gd_3Al_5O_{12}$, $Tb_3Al_5O_{12}$ and $Lu_3Al_5O_{12}$ Single Crystals. *J. Phys. Chem. Solids* **2003**, *64*, 599–605. [CrossRef]
28. Tang, F.; Cao, Y.; Huang, J.; Liu, H.; Guo, W.; Wang, W. Fabrication and Laser Behavior of Composite Yb:YAG Ceramic. *J. Am. Ceram. Soc.* **2012**, *95*, 56–69. [CrossRef]
29. Tauc, J. Optical Properties and Electronic Structure of Amorphous Ge and Si. *Mater. Res. Bull.* **1968**, *3*, 37–46. [CrossRef]
30. Xu, Y.; Ching, W.Y. Electronic Structure of Yttrium Aluminum Garnet. *Phys. Rev. B* **1999**, *59*, 10530. [CrossRef]
31. Jubu, P.R.; Yam, F.K.; Igba, V.M.; Beh, K.P. Tauc-Plot Scale and Extrapolation Effect on Bandgap Estimation from UV–Vis–NIR Data—A Case Study of β-Ga2O3. *J. Solid. State Chem.* **2020**, *290*, 121576. [CrossRef]
32. Brik, M.G.; Srivastava, A.M.; Popov, A.I. A Few Common Misconceptions in the Interpretation of Experimental Spectroscopic Data. *Opt. Mater.* **2022**, *127*, 112276. [CrossRef]
33. Aull, B.F.; Jenssen, H.P. Vibronic Interactions in Nd: YAG Resulting in Nonreciprocity of Absorption and Stimulated Emission Cross Sections. *IEEE J. Quantum Electron.* **1982**, *18*, 925–930. [CrossRef]

34. Fan, T.Y.; Wynne, R.; Daneu, J.L. Thermal Coefficients of the Expansion and Refractive Index in YAG. *Appl. Opt.* **1999**, *38*, 3282–3284.
35. Payne, S.A.; Chase, L.L.; Smith, L.K.; Kway, W.L.; Wyers, W.F. Infrared Cross-Section Measurements for Crystals Doped with Er^{3+}, Tm^{3+}, and Ho^{3+}. *IEEE J. Quantum Electron.* **1992**, *28*, 2619–2630. [CrossRef]